The background of the cover is a dark field filled with numerous circular and irregular shapes, each representing a lipid vesicle. These vesicles are outlined in a bright red color. Inside many of the vesicles, there are intricate, branching, and interconnected patterns of red lines, which represent flexible nanotubes that have formed within the vesicles. The overall appearance is that of a complex, self-organizing system. The title 'ADVANCED MATERIALS INTERFACES' is overlaid on the top right of the image. 'ADVANCED' and 'MATERIALS' are in a bold, green, sans-serif font, while 'INTERFACES' is in a bold, yellow, sans-serif font.

# ADVANCED MATERIALS INTERFACES

## LIPID MEMBRANES

The lipid membranes of giant vesicles form patterns of flexible nanotubes when exposed to aqueous polymer solutions. The tubes point towards the solutions with the higher PEG concentration and reveal a large spontaneous curvature that the membranes acquire via asymmetric PEG adsorption. Recent studies are reviewed by Rumiana Dimova and Reinhard Lipowsky in article 1600451.

# Giant Vesicles Exposed to Aqueous Two-Phase Systems: Membrane Wetting, Budding Processes, and Spontaneous Tubulation

Rumiana Dimova\* and Reinhard Lipowsky\*

In this review, we describe recent studies of giant unilamellar vesicles exposed to aqueous polymer solutions. These solutions undergo phase separation when the weight fractions of the polymers exceed a few percent. Depending on the lipid and polymer composition, the membrane may be completely or partially wetted by the aqueous phases. The deflation process induces a variety of vesicle shape transformations. One such transformation is droplet-induced budding of the vesicles. Another, particularly striking transformation is the spontaneous tube formation, which reveals a substantial asymmetry and spontaneous curvature of the membranes, arising from the different polymer compositions across the membrane. The tubulation starts with the nucleation of small membrane buds which then grow into necklace-like tubes. When the tube length reaches a certain critical value, the necklace-like tube transforms into a cylindrical one. Analyzing different aspects of the observed vesicle shapes, quantitative estimates of the spontaneous curvature which is found to vary, depending on the lipid composition, between  $1/(125\text{ nm})$  and  $1/(600\text{ nm})$ , are obtained. These curvatures are generated by the weak adsorption of poly(ethylene glycol) (PEG) molecules onto the lipid membranes, with a relatively small binding affinity of about  $4\text{ kJ mol}^{-1}$  or  $1.6 k_B T$  per PEG molecule for either liquid-ordered or liquid-disordered membranes.

## 1. Introduction

Giant unilamellar vesicles (GUVs)<sup>[1]</sup> provide simple model systems for cell membranes and are often used to construct biomimetic cellular compartments. Cell membranes are exposed to the cytosol which contains many macromolecules such as proteins, nucleic acids, and polysaccharides. This crowded environment can be mimicked, to some extent, by aqueous two-phase systems consisting of aqueous polymer solutions. Such systems have been frequently used in biochemical analysis and biotechnology<sup>[2]</sup> to separate and purify biomolecules, cell organelles, and cell membranes. One such system that has been employed for a long time is provided by the aqueous solution

of poly(ethylene glycol) (PEG) and dextran. This solution undergoes phase separation when the polymer concentrations exceed a few weight percent.

The study of aqueous phase separation within GUVs was initiated by the group of C. Keating,<sup>[3]</sup> as a model system for biological microcompartmentation, and was used to investigate protein redistribution between the different phases.<sup>[4]</sup> In the last couple of years, these lipid-polymer systems have been intensely studied, both experimentally and theoretically, and were shown to lead to a variety of interesting phenomena: complete and partial wetting of the membranes by the aqueous phases,<sup>[5]</sup> droplet-induced budding of vesicles arising from partial membrane wetting,<sup>[5b,c]</sup> droplet fission in vesicles,<sup>[6]</sup> and spontaneous formation of membrane nanotubes.<sup>[7]</sup> The latter process reveals that the vesicle membrane has acquired a large spontaneous curvature which is generated by the solution asymmetry across the lipid bilayer. In the following, we will review

the nucleation and growth of nanotubes, their necklace-like and cylindrical morphologies, and the associated methods to determine the spontaneous curvature in a quantitative manner.

To begin with, we briefly review the different membrane-associated effects of the PEG-dextran solutions, focusing in particular on the wetting behavior of the membranes in contact with the aqueous phases,<sup>[5]</sup> on the droplet-induced budding associated with partial wetting,<sup>[5b,c,7a]</sup> and on the different morphologies of tubulated vesicles.<sup>[7]</sup> We first discuss the phase diagram of the PEG-dextran solutions and describe our method to induce phase separation within the vesicles by osmotic deflation. We then characterize complete and partial wetting of the membrane by the PEG-rich phase and emphasize that the lipid-polymer system undergoes a complete-to-partial wetting transition. The partial wetting geometries involve three effective contact angles which can be directly observed in the optical microscope. Using these angles, one can calculate the intrinsic contact angle which represents a hidden material parameter of the system. Depending on the phase behavior of the aqueous two-phase system, the vesicles exhibit three different morphologies with nanotubes. The tubes are nucleated from small

Dr. R. Dimova, Prof. R. Lipowsky  
Max Planck Institute of Colloids and Interfaces  
Science Park Golm  
14424 Potsdam, Germany  
E-mail: dimova@mpikg.mpg.de;  
lipowsky@mpikg.mpg.de



DOI: 10.1002/admi.201600451

membrane buds which subsequently grow into necklace-like tubes. These tubes continue to grow in length until they reach a critical tube length and transform into cylindrical tubes. Three different methods of image analysis were used to deduce the spontaneous curvature of the membranes and gave rather consistent results. The membrane curvature is generated locally by the weak adsorption of PEG molecules as follows from general theoretical considerations, corroborated by molecular dynamics simulations and preliminary tubulation experiments with PEG alone. Finally, we discuss some related aspects that may be relevant for processes in the living cell.

## 2. Phase Separation in the PEG–Dextran Solutions: Binodals and Tie Lines

The phenomenon of phase separation is often observed in solutions of two polymer species. It also applies in general to polymeric solutes such as proteins and nucleic acids. One of these aqueous two-phase systems (ATPSs) that has been studied in great detail is provided by aqueous polymer mixtures of PEG and dextran. This ATPS has been widely used for the separation of biomolecules, viruses, and cells.<sup>[2,8]</sup> Other systems based on synthetic polymers, polysaccharides, or proteins have also been developed and applied in biotechnology for biomolecule separation.<sup>[9]</sup> In solutions of two oppositely charged polyelectrolytes, a more complex phase behavior can be observed.<sup>[10]</sup> For systems with more than two types of neutral polymers, additional phases may also be formed. Even single-polymer solutions may separate into a polymer-poor and a polymer-rich phase under specific temperature or salt conditions.

Above a certain concentration, PEG–dextran solutions form two aqueous phases which are in equilibrium with each other, see the phase diagram in **Figure 1**. The binodal curve divides this phase diagram into two regions, a one-phase region at relatively low weight fractions of the polymers and a two-phase coexistence region at higher polymer concentrations. When one prepares a PEG–dextran solution with weight fractions corresponding to the coexistence region, the solution separates into two aqueous phases that differ in their composition, density, and viscosity. The lighter (upper) phase is characterized by a higher fraction of PEG while the denser (lower) phase is dextran-rich. The PEG-rich phase has a lower refractive index compared to the dextran-rich phase, which makes the two phases easily distinguishable when observed in giant vesicles with phase contrast microscopy, see for example, **Figure 2h–k**. The polymer compositions of the two coexisting phases correspond to the end points of the tie lines in **Figure 1**. The phase diagram also contains a critical point at which the tension of the interface between the PEG-rich and the dextran-rich phase vanishes. The range of interfacial tensions that was accessible in our experiments covers several orders of magnitude, from sub  $\mu\text{N m}^{-1}$  to sub  $\text{mN m}^{-1}$  values depending on the distance from the critical point.<sup>[11]</sup> Thus, this system can provide a particularly mild environment for biomolecules and the low interfacial tension is probably the reason why these molecules do not denature even when they adsorb selectively to the liquid–liquid interface.



**Rumiana Dimova** obtained her Ph.D. at Bordeaux University (France) in 1999. Afterward she joined the Max Planck Institute of Colloids and Interfaces as a post-doctoral fellow, where she became a group leader in 2000. Since then she leads the Biomembrane lab in the Department of Theory and BioSystems. Her main research interests are in the field of membrane biophysics. In 2014, she was awarded with the EPS Emmy Noether distinction for women in physics.



**Reinhard Lipowsky** obtained his Ph.D. in 1982 at the University of Munich. In 1990, he was appointed full professor at the University of Cologne and director at the Forschungszentrum Jülich. Since 1993, he is a director at the Max Planck Institute of Colloids and Interfaces. He works on fundamental aspects of biomimetic and biological systems.

A number of different methods have been applied to measure the binodal and determine the tie lines in ATPSs, see, for example, ref. [12] Recently, we proposed a relatively simple approach based on density measurements;<sup>[11a]</sup> the resulting binodal and tie lines are displayed in **Figure 1**.

Whereas the binodal line is easily accessible, for example, via cloud-point titration, the location of the tie lines is more difficult to measure because the polymers are usually not monodisperse. To assess the polymer concentrations in the two coexisting phases, one typically measures two physical properties, e.g., optical rotation and refractive index, of both phases.<sup>[9b]</sup> The dextran concentration in the phase is determined by a polarimeter, while the PEG concentration is obtained after subtracting the dextran contribution to the refractive index. A gravimetric method was introduced to determine the tie line of ATPS containing PEG and salt, by measuring the weight of two coexisting phases and forcing the tie-line end points to lie on a predetermined binodal.<sup>[13]</sup> Some care must be taken, however, when applying this method to PEG–dextran solutions because of the polydispersity of commercially available dextran, which leads to a mismatch between the end points of the tie line and the binodal. This mismatch, which is absent for monodisperse polymers, reflects the fractionation of the dextran molecules, i.e., the different size distributions of these molecules within the two phases.<sup>[14]</sup>

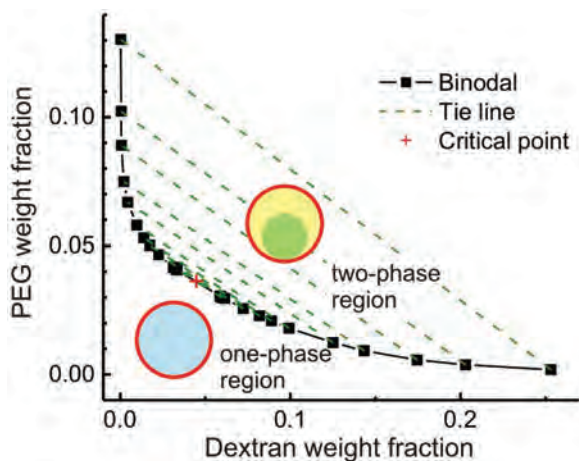


**Figure 1.** Binodal (black squares) and tie lines (green dashed lines) of the aqueous solution of dextran (molecular weight between 400 and 500 kg mol<sup>-1</sup>) and PEG (molecular weight of 8 kg mol<sup>-1</sup>) measured at 24 ± 0.5 °C.<sup>[17a]</sup> The red cross indicates the location of the critical point. Below the binodal, the polymer solution is homogeneous; above the binodal it undergoes phase separation. The insets illustrate the vesicle morphologies with the membrane (red) enclosing the homogeneous solution (blue) or the two liquid droplets consisting of dextran-rich (green) and PEG-rich (yellow) phases. Reproduced with permission.<sup>[17d]</sup> Copyright 2012, Royal Society of Chemistry.

Recently, we investigated an ATPS with a broad molar mass distribution for dextran and a narrow molar mass distribution for PEG.<sup>[15]</sup> The phases were separated and their composition was studied by gel permeation chromatography. The data showed that the high molar mass components of dextran were enriched in the dextran-rich phase and depleted from the PEG-rich phase whereas the molar mass distribution of PEG was rather similar in both phases. For a given molar mass or chain length of dextran, the fractionation degree was characterized by the ratio of the dextran concentration in the PEG-rich phase to the dextran concentration in the dextran-rich phase and was found to depend exponentially on the chain length.

### 3. Aqueous Two-Phase Separation within Giant Vesicles: Wetting Phenomena

The phase separation process of ATPS encapsulated in GUVs can be induced in two ways. One approach is based on temperature changes<sup>[3,4,6,16]</sup> and the shift of the binodal with temperature. The second approach, which was introduced by our group, induces phase separation via osmotic deflation of the vesicles.<sup>[5a,7a,c]</sup> The polymer concentration within the vesicles is raised above the binodal by exposing the vesicles to a hypertonic medium. Water is forced out of the vesicle to balance the resulting osmotic pressure, leading to an increase in the polymer concentration and to phase separation within the vesicles. Even though all vesicles are formed in the presence of the same single-phase aqueous polymer solution, both the temperature and the deflation method may lead to vesicle-to-vesicle variations in the enclosed polymer solutions depending on the vesicle history and on the polydispersity of the polymers. Dextran of higher molecular weight have

a tendency to get encapsulated less efficiently than those of lower molecular weight.<sup>[17]</sup>

In principle, the confinement of an ATPS to the volume of a vesicle leads to finite size effects on the phase diagram but for the GUVs used here, which had a linear size of tens of micrometers, such effects are expected to be small and were not detectable within the accuracy of our measurements. Finite size effects should be much stronger for the confinement of an ATPS to large unilamellar vesicles (LUVs) which have a linear size of about 100 nm but the latter systems have not been considered here.

#### 3.1. Wetting Transition

Phase separation within a GUV leads to a dextran-rich droplet sitting at the vesicle bottom and a PEG-rich droplet filling the rest of the vesicle. Depending on the degree of deflation and the interaction of the two aqueous phases with the membrane, different morphologies can be observed: a single sphere, two partial spherical caps, and two spheres connected by a membrane neck as illustrated in Figure 2a. In practice, observations of the overall vesicle shape have been made as vertical cross sections using a confocal microscope as shown in Figure 2b–e,i–p or by horizontally aligning a microscope to allow for side-view phase contrast observations as in Figure 2h–k.

In general, liquid droplets at interfaces may exhibit zero or nonzero contact angles corresponding to complete or partial wetting, respectively. As one varies a certain control parameter such as temperature or liquid composition, the system may undergo an interfacial phase transition from complete to partial wetting. It is important to note that such a phase transition requires only small changes of the control parameters and does not require any changes of the underlying molecular interactions. For PEG–dextran solutions in contact with lipid bilayers, we observed complete-to-partial wetting transitions for a variety of lipid compositions.<sup>[5a,7c]</sup> The first observation of this kind is shown in Figure 2c,d.

For a tense vesicle with no excess area, the dextran-rich phase, which is denser than the PEG-rich phase, sits at the vesicle bottom as a quasi-spherical droplet, see Figure 2c (in the absence of gravity, the dextran-rich phase would form a spherical droplet that has no contact with the vesicle membrane). In the case of partial wetting, the dextran-rich droplet adopts the shape of a lens as in Figure 2d,e. When the vesicle volume has been reduced and the dextran-rich phase partially wets the membrane, the vesicle deforms into a dumbbell shape as in Figure 2j,k.

For partial wetting, the vesicle membrane consists of two different segments that are in contact with the PEG-rich and the dextran-rich phase. Both membrane segments and the interface between the two liquid phases form spherical caps to a very good approximation. The force balance along the contact line then leads to three equations for the three effective contact angles which can be combined into the two equations  $\hat{\Sigma}_{pe} = \Sigma_{pd} \sin\theta_d / \sin\theta_e$  and  $\hat{\Sigma}_{de} = \Sigma_{pd} \sin\theta_p / \sin\theta_e$ .<sup>[7a,b]</sup> Here,  $\hat{\Sigma}_{pe}$  and  $\hat{\Sigma}_{de}$  are the tensions of the pe and de membrane segments in contact with the PEG-rich and the dextran-rich phase, respectively, and  $\Sigma_{pd}$  is the tension of the interface between the

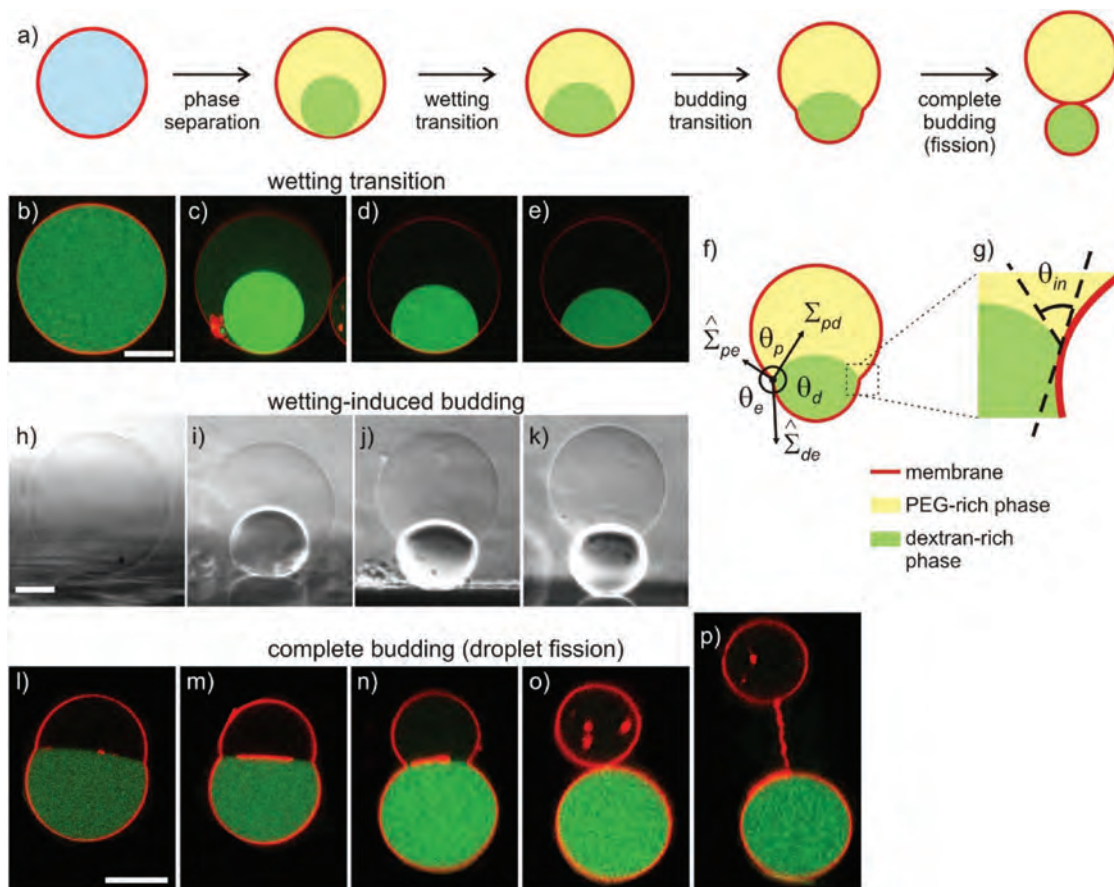


**Figure 2.** Response of ATPS-loaded vesicles when exposed to osmotic deflation. a) Schematic illustration of the processes induced by the deflation: phase separation within the vesicle, wetting transition, vesicle budding, and fission of the enclosed phases into two membrane-enclosed droplets. b–e, l–p) Confocal images of fluorescently labeled vesicles can be used to show the morphological transformation of the membrane (false color red) and the enclosed droplets and their wettability of the membrane. Here, a small fraction of the dextran is labeled (false color green). Since the latter phase has the larger mass density, the dextran-rich droplet is located beneath the PEG-rich one. c, d) As the external osmolarity is increased the system undergoes a complete-to-partial wetting transition. Adapted with permission.<sup>[5a]</sup> Copyright 2008, American Chemical Society. In the sketch in (f), the three effective contact angles as observed with optical microscopy are indicated as well as the two membrane tensions and the interfacial tension  $\Sigma_{pd}$ .<sup>[5b,7b]</sup> The contact line is indicated by the circled dot  $\odot$ . The intrinsic contact angle  $\theta_{in}$ , which characterizes the wetting properties of the membrane by the PEG-rich phase at the nanometer scale, is sketched in (g). h–k) Side-view phase contrast images of a vesicle sitting on a glass substrate and loaded with PEG–dextran ATPS. h, i) After phase separation, the interior solution consists of two liquid droplets corresponding to a PEG-rich and dextran-rich phase, respectively. j, k) Further deflation of the vesicle causes the dextran-rich droplet to bud out. Adapted with permission.<sup>[7a]</sup> Copyright 2011, National Academy of Sciences. l–p) Significant deflation of a vesicle enclosing two liquid phases can lead to bulging of one of the phases from the vesicle body and fission of the enclosed droplets.<sup>[5c]</sup> Scale bars correspond to 25  $\mu\text{m}$ .

two polymer phases (pd). Using these relations and fitting the contours of the two membrane segments and the interface by circular segments, the membrane tensions can be determined from the contact angles.

### 3.2. Wetting- or Droplet-Induced Budding

When both encapsulated phases partially wet the membrane, the smaller one may bud out of the vesicle body upon further deflation. Figure 2h–n shows two such examples. The vesicles with two liquid phases are approximately spherical at low osmolarity ratio between the external medium and the initial internal polymer solution, see Figure 2h. When the vesicles are further deflated, the dextran-rich phase starts to form a bud away from the PEG-rich phase, see Figure 2j–n. The excess area arising

from deflation is utilized by the vesicle to undergo morphological changes and a budding process.<sup>[5b,c]</sup> In this way, the area of the liquid two-phase interface is decreased significantly. As the osmolarity of the medium is increased further, the dextran-rich phase may form a complete bud<sup>[5c,6]</sup> leading to a dumbbell-like vesicle where the area of the two-phase interface is almost zero, see last cartoon in Figure 2a and images in Figure 2o, p. The budding direction can be reversed if the phase separation occurs in the exterior aqueous compartment,<sup>[5c]</sup> see example in Figure 3.

In mechanical equilibrium, the two membrane tensions  $\hat{\Sigma}_{pe}$  and  $\hat{\Sigma}_{de}$  must be balanced along the contact line (where the external medium, the PEG-rich phase, and the dextran-rich phase are in proximity) by the interfacial tension  $\Sigma_{pd}$  between the two liquid phases, see Figure 2f and the previous subsection.<sup>[5b,7a,b]</sup> The interfacial tension  $\Sigma_{pd}$  pulls on the

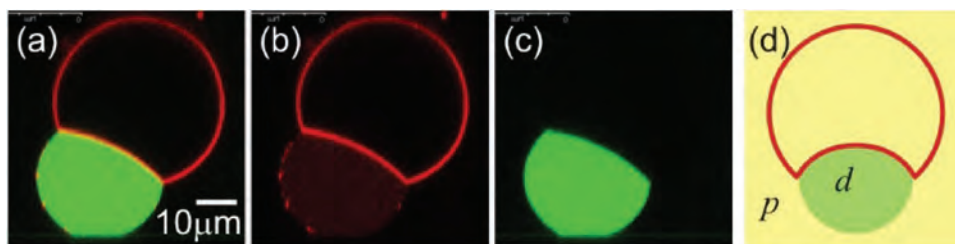


**Figure 3.** Inward budding of a vesicle in contact with two aqueous solutions. a–c) xz-confocal scans and d) a cartoon of a vesicle with fluorescently labeled membrane (red) in contact with a dextran-rich droplet (false color green) and the PEG-rich bulk phase. The confocal images in (a)–(c) show the mixed fluorescence signal, and the red and green channels separately. In the cartoon, the dextran-rich droplet (green) is denoted by *d* and the PEG-rich phase (yellow) by *p*. Adapted with permission.<sup>[5c]</sup> Copyright 2012, American Chemical Society.

membrane toward the vesicle interior for vesicles enclosing phase-separated droplets as in Figure 2 or toward the vesicle exterior if the phase separation occurs outside the vesicle and both phases wet the membrane as in Figure 3. The precise pulling direction depends on the intrinsic contact angle which is defined in the next subsection and attains a nonzero value for partial wetting. For partial wetting with a small interfacial tension  $\Sigma_{pd}$ , the shape deformation of the vesicle membrane induced by this tension is small as well and the vesicle shape as viewed in the optical microscope remains approximately spherical. The excess area arising from deflation can be stored in the form of nanotubes<sup>[7]</sup> as we will discuss further below. As the vesicle is further deflated, the interfacial tension  $\Sigma_{pd}$  increases and the associated shape deformation of the membrane becomes visible in the optical microscope. The overall shape is then determined by the volumes of the two aqueous droplets, by the interfacial free energy of the *pd* interface between these droplets, and by the total area of the vesicle membrane which includes the membrane area of the nanotubes. In many cases, one then observes budding of the dextran-rich phase which significantly reduces the interfacial energy by decreasing the contact area between the two aqueous droplets.

### 3.3. Intrinsic Contact Angle

When viewed with optical resolution, the membrane of budded vesicles as in Figures 2j–n and 3a,b exhibits a kink along the contact line, see sketches in Figures 2f and 3d. However, if the membrane shape had a kink that persisted to smaller length scales, its bending energy would become infinite. Therefore, when viewed with suboptical resolution, the membrane should be smoothly curved, which implies the existence of an intrinsic contact angle  $\theta_{in}$  as sketched in Figure 2g.<sup>[5b]</sup> Indeed, minimization of the membrane's bending energy together with the force balance along the three phase contact line shows that the intrinsic angle is related to the effective contact angles via  $\cos \theta_{in} = (\sin \theta_p - \sin \theta_d) / \sin \theta_e$ . Here,  $\theta_d$ ,  $\theta_p$ , and  $\theta_e$  are the effective contact angles (as in Figure 2f), which can be obtained from the microscopy images. Thus,  $\theta_{in}$  can be determined from experimentally measurable parameters; results for various phase and membrane compositions are reported in refs. [5b,c] and [7c]. Whereas the effective contact angles depend on the vesicle geometry, the intrinsic contact angle is a material parameter, which arises from the molecular interactions between

the phases and the membrane. The intrinsic contact angle  $\theta_{in}$  becomes equal to the effective contact angle  $\theta_p$  whenever the membrane is locally flat with  $\theta_e = 180^\circ$ . One example for this simplification and the resulting equality  $\theta_{in} = \theta_p$  is provided by the geometry in Figure 2c–e. A sessile PEG-rich droplet in contact with a supported bilayer would provide another example for this equality. In the latter case, the force balance along the contact line also involves the adhesion free energy of the bilayer with the substrate surface. Supported lipid membranes often represent bilayers that experience relatively high tensions close to their lysis tension. In this tension regime, the molecular interface at the membrane surface will change and thus affect the interaction with the aqueous phases, which in turn will be reflected in the intrinsic contact angle. Therefore, measurements with sessile droplets may reveal the effects of membrane tension on the intrinsic contact angle  $\theta_{in}$ .

## 4. Tubulation of Membranes with Uniform Lipid Composition

In the absence of external pulling forces, the spontaneous tubulation of vesicles reveals the presence of a substantial spontaneous curvature, which is large compared to the inverse vesicle size.<sup>[7b]</sup> Therefore, the spontaneous tubulation of giant vesicles in contact with a phase-separated PEG–dextran solution as observed in ref. [7a] should primarily reflect the spontaneous curvature of the membranes rather than the phase separation process itself. Indeed, our most recent study<sup>[7c]</sup> has shown that the membrane tubes are formed already in the aqueous one-phase region.

### 4.1. Different Patterns of Flexible Nanotubes

Three types of nanotube patterns have been observed for vesicles exposed to PEG–dextran solutions, corresponding to three different vesicle morphologies as shown schematically in Figure 4.<sup>[7c]</sup> These different morphologies were obtained by osmotic deflation of the vesicles, thereby exposing the two bilayer leaflets to polymer solutions of different composition. The vesicle membranes were composed of dioleoylphosphatidylcholine (DOPC), dipalmitoylphosphatidylcholine (DPPC), and cholesterol. Two different lipid compositions were studied in detail, corresponding either

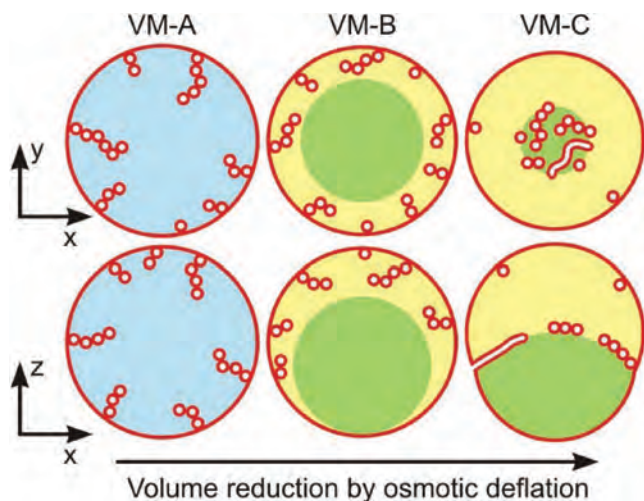


**Figure 4.** Three nanotube patterns corresponding to the distinct vesicle morphologies VM-A, VM-B, and VM-C which are successively observed when the vesicle volume is reduced by osmotic deflation: Schematic views of horizontal  $xy$ -scans (top row) and of vertical  $xz$ -scans (bottom row) across the deflated vesicles. In all cases, the tubes are filled with external medium (white). For the morphology VM-A, the interior polymer solution is uniform (blue), whereas it is phase separated (green-yellow) for the morphologies VM-B and VM-C, with complete and partial wetting, respectively, of the membrane by the PEG-rich aqueous phase (yellow). For the VM-B morphology, the nanotubes explore the whole PEG-rich (yellow) droplet but stay away from the dextran-rich (green) one. For the VM-C morphology, the nanotubes adhere to the pd interface between the two aqueous droplets forming a thin and crowded tube layer along this interface. Adapted with permission.<sup>[7c]</sup> Copyright 2016, American Chemical Society.

to a liquid-ordered (Lo) or a liquid-disordered (Ld) phase of the membrane. The composition of the Lo vesicles was DOPC:DPPC:cholesterol = 13:44:43 (mole fractions) and that of the Ld vesicles was DOPC:DPPC:cholesterol = 64:15:21. The Ld membranes were more flexible than Lo membranes, with the bending rigidity  $\kappa_{Lo}$  of the Lo membranes being about 4.5 times larger than the bending rigidity  $\kappa_{Ld}$  of the Ld membranes.<sup>[18]</sup>

Initially, the vesicles were spherical and enclosed a homogeneous PEG–dextran solution. These vesicles were then deflated osmotically by using exterior solutions that contained fixed weight fractions of the two polymers but an increasing amount of sucrose. After the first deflation step, the interior polymer solution still formed a uniform aqueous phase, corresponding to the VM-A morphology in Figure 4. After the second and all subsequent deflation steps, the interior solution underwent phase separation into a PEG-rich and a dextran-rich phase, which formed two aqueous droplets within the vesicles. The PEG-rich droplet was always in contact with the membranes whereas the dextran-rich droplet came into contact with the Ld and Lo membranes only after the third and fourth deflation steps, respectively. When the dextran-rich phase was not in contact with the membranes, these membranes were completely wetted by the PEG-rich phase, which defines the vesicle morphology VM-B. Because the dextran-rich phase has a larger mass density than the PEG-rich phase, the dextran-rich droplets sank to the bottom of the vesicle as shown in Figure 4. In a gravity-free environment the VM-B morphology would be char-

acterized by a dextran-rich droplet, floating freely within the PEG-rich phase. When the dextran-rich phase came into contact with the membranes, the membranes were partially wetted by both aqueous phases, corresponding to the vesicle morphology VM-C for which the pd interface and the segments of the vesicle membrane formed nonzero contact angles, see Figure 2f. Therefore, the deflation path crossed a complete-to-partial wetting transition that was located between the second and third deflation step for the Ld membranes and between the third and fourth deflation step for the Lo membranes. Because of the different wetting properties, the nanotube patterns observed for the VM-B and VM-C morphologies are quite different as illustrated by the confocal images in Figure 5.

Each osmotic deflation step reduces the vesicle volume and, thus, increases the area-to-volume ratio of the vesicle. In the absence of polymers, vesicles undergo smooth shape transformations from spherical toward prolate shapes as studied previously for one-component membranes and relatively small values of the spontaneous curvature<sup>[19]</sup> which are of the order of the inverse vesicle size. In contrast to such conventional shape transformations, the vesicles studied in ref. [7c] adopted a spherical shape after the initial deflation steps, both for the flexible Ld and the more rigid Lo membranes. However, because the vesicle volume was reduced by the deflation, the spherical mother vesicles had an *apparent* area  $A_{app}$  that was smaller than the initial vesicle area  $A_0$ . The missing membrane area,  $A = A_0 - A_{app}$ , was stored in nanotubes that protruded into the vesicle interior. Performing several deflation steps, up to 15% of the vesicle area could be stored in tubes.<sup>[7a,c]</sup> The tubes had a width that was much smaller than the size of the vesicles which implies that the spontaneous curvature of the vesicle membranes was much larger than the inverse size of the membranes.

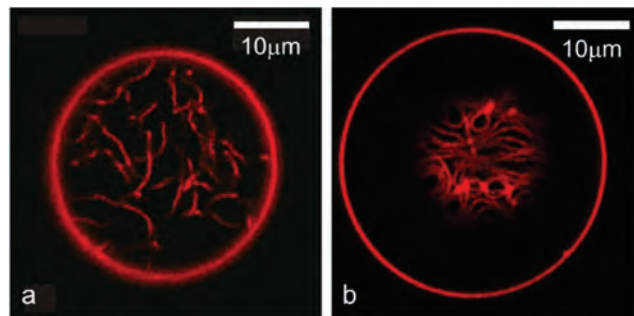


**Figure 5.** Patterns of flexible nanotubes formed by Ld membranes, corresponding to complete and partial wetting of the membranes by the PEG-rich phase:<sup>[7c]</sup> a) Disordered pattern corresponding to an  $xy$ -scan of the VM-B morphology. Because the Ld membrane is completely wetted by the PEG-rich phase, the nanotubes explore the whole PEG-rich droplet but stay away from the dextran-rich phase and b) layer of densely packed tubes as visible in an  $xy$ -scan of the VM-C morphology. As a result of partial wetting, the nanotubes now adhere to the pd interface between the two aqueous droplets and form a thin layer in which crowding leads to short-range orientational order of the tubes. Note that the tube layer is only partially visible in the confocal image of (b) because the pd interface is curved into a spherical cap. In both (a) and (b), the diameter of the tubes is below the diffraction limit but the tubes are theoretically predicted to be necklace-like and cylindrical in panels (a) and (b), respectively. Reproduced with permission.<sup>[7c]</sup> Copyright 2016, American Chemical Society.

## 4.2. Nucleation and Growth of Necklace-Like Tubes

The tubes of the Lo membranes were sufficiently thick to determine their morphologies directly from the confocal images. The 3D scans show that each Lo vesicle contains many necklace-like tubes consisting of quasi-spherical membrane beads connected by narrow membrane necks. The presence of these tubes can be explained theoretically by the competition of two kinetic pathways which are related to two different bifurcations of the vesicle shape. Initial deflation of a spherical vesicle leads, via an oblate-stomatocyte bifurcation,<sup>[19]</sup> to the formation of a single spherical bud protruding into the vesicle interior. Upon further volume reduction, the vesicle can follow two alternative pathways depending on the lipid flow through the narrow membrane neck between the bud and the mother vesicle. If this flow is relatively fast, the bud grows in size until it transforms, via a sphere-to-prolate bifurcation, into a short necklace of two identical spheres.

As we continue to deflate the vesicle, the “fast-flow” pathway acts to elongate the necklace-like tube, which then passes through a series of necklace-like morphologies that consist of an increasing number of small spheres connected by narrow membrane necks. The corresponding free energy landscape has been determined by minimizing the bending energy of the membrane within the spontaneous curvature model.<sup>[7c]</sup> On the other hand, if the lipid flow through the neck is relatively slow or blocked, the mother vesicle uses the excess area released during the deflation process to form a second bud. Therefore, the deflation of the vesicle generates new buds via the “slow-flow” pathway, which are then elongated into necklace-like tubes via the “fast-flow” pathway. The competition between these two pathways generates a large number of buds and necklace-like tubes as experimentally observed during the initial deflation steps.

The two pathways just described provide a plausible but simplified view of the kinetics. On the one hand, the energy landscape obtained by minimizing the bending energy of the vesicle membrane involves many branches of metastable states. On the other hand, thermal fluctuations will also play an important role for the nucleation of buds and tubes. Indeed, a large spontaneous curvature should promote asymmetric, spatially localized shape fluctuations. Such a fluctuation may generate new buds or may add membrane area to existing buds or tubes. In this way, shape fluctuations provide a local mechanism for tube nucleation and growth which does not follow the global minimization of the bending energy.

## 4.3. Transformation from Necklace-Like to Cylindrical Tubes

Even though the vast majority of the tubes were necklace-like, we also observed cylindrical tubes for the VM-C morphology of Lo membranes. Somewhat surprisingly, both necklace-like and cylindrical tubes were found to coexist on the same vesicle. One example is provided by the vesicle with Lo membrane displayed in **Figure 6**. The confocal images obtained for this vesicle revealed the existence of a couple of long cylindrical tubes that spiral around the spherical cap of the pd interface. These observations can be understood from the

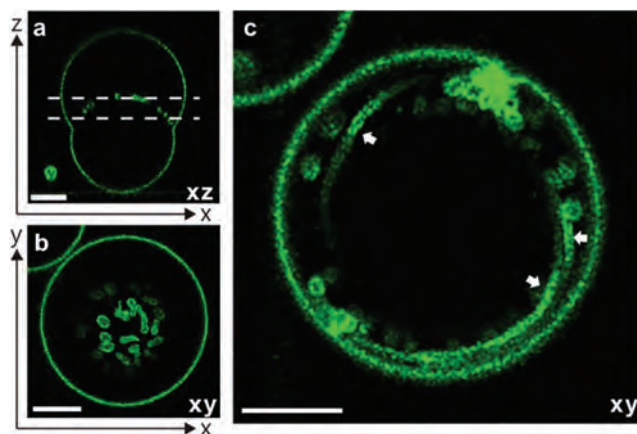


**Figure 6.** Necklace-cylinder coexistence for giant vesicle with Lo membrane:<sup>[7c]</sup> a) Confocal *xz*-scan; b) confocal *xy*-scan at a height corresponding to the upper dashed line in panel (a); c) confocal *xy*-scan at a height corresponding to the lower dashed line in panel (a). This cross section reveals the coexistence of several long cylindrical segments (white arrows) and several short necklace-like tubes. All scale bars are 10  $\mu\text{m}$ .

competition of different energy contributions, which favor necklace-like tubes below a certain critical tube length but cylindrical tubes above this length. At the critical tube length, the necklace-like tube transforms into a cylindrical one. Such a transformation can proceed in a continuous manner via intermediate unduloids.

For the VM-A and VM-B morphologies, the existence of a critical tube length can be understood intuitively from the following simple argument. If the membrane has spontaneous curvature  $m$ , a necklace-like tube consisting of small spheres with radius  $R_{ss} = 1/|m|$  connected by closed membrane necks has vanishing bending energy. For a cylindrical tube with radius  $R_{cy} = 1/(2|m|)$ , the main body of the cylinder has vanishing bending energy as well but such a tube must be closed by at least one end cap. In fact, in order to obtain a well-defined connection between the cylinder and the mother vesicle, we include a second end cap that is connected to the mother vesicle via a closed neck. The closed neck is stable because it fulfills the stability condition  $M_{cap} + 1/R_{ls} = 2m + 1/R_{ls} > 2m$  which depends on the mean curvature  $M_{cap} = 2m$  of the end cap and the mean curvature  $1/R_{ls}$  of the large spherical vesicle.<sup>[20]</sup> The two end caps have the finite bending energy  $2\pi\kappa$ , with the bending rigidity  $\kappa$  being typically of the order of  $10^{-19}$  J or  $20 k_B T$  at room temperature. Therefore, the bending energy of the spherical caps disfavors the cylindrical tube. On the other hand, the necklace-like tube has a larger volume compared to the cylindrical one and the osmotic pressure difference across the membranes acts to compress the tubes when they protrude into the interior solution within the vesicles.<sup>[7b]</sup> Therefore, such a tube can lower its free energy by reducing its volume, which favors the cylindrical tube. The volume work is proportional to the tube length whereas the bending energy of the end caps is independent of this length. The competition between these two energies then implies that short tubes are necklace-like whereas long tubes are cylindrical.

The same conclusion is obtained by minimizing the bending energy of the whole vesicle for the VM-A and VM-B

morphologies.<sup>[7c]</sup> One then finds that, for fixed vesicle volume and membrane area, the mother vesicle has a smaller bending energy when it forms a cylindrical tube and that this energy decrease of the mother vesicle overcomes the bending energy increase via the spherical end caps when the cylindrical tube is sufficiently long. The critical tube length at which the necklace-like tube transforms into a cylindrical one is about three times the vesicle radius.

For the VM-C morphology, the nanotubes adhere to the pd interface. In this situation, the critical tube length is primarily determined by the interplay between (i) the adhesion energy, which is proportional to tube length and favors the cylindrical tube and (ii) the bending energy of the end caps for the cylindrical tube, which disfavors the latter tube. Energy minimization now leads to a critical tube length that depends on four material parameters, namely, the bending rigidity, the spontaneous curvature, the interfacial tension of the pd interface, and the intrinsic contact angle of the PEG-rich droplet with the vesicle membrane, all of which have been determined experimentally.<sup>[7c]</sup> Using the measured values of these parameters, one concludes that the Ld tubes in Figure 5b are sufficiently long to attain a cylindrical shape.

#### 4.4. Universal Morphological Features of Spontaneous Tubulation

The theory developed in ref. [7c] revealed that the experimentally observed tubes were nucleated from small buds, which subsequently grew into necklace-like tubes. Depending on the kinetics of the budding and growth processes, further deflation can lead to additional buds or to the extension of existing buds and necklace-like tubes. The latter tubes grow until they transform into cylinders when their length exceeds a certain critical value. This critical length can be reduced by the presence of a liquid–liquid interface to which the nanotubes adhere because of partial wetting. These morphological features are universal and apply to the spontaneous tubulation of membranes irrespective of the lipid composition and the underlying molecular mechanism for curvature generation.

### 5. Spontaneous Curvature from Systematic Image Analysis

In order to determine the membrane spontaneous curvature revealed by the spontaneous tubulation of the Ld and Lo membranes, we developed three different and independent methods of image analysis.<sup>[7c]</sup> All three methods gave very consistent results for both types of membranes when applied to the three vesicle morphologies depicted in Figure 4.

#### 5.1. Direct Shape Analysis of Membrane Tubes

For the Lo membranes, the tube had a diameter well above optical resolution, which made it possible to directly deduce the shape of the tubes from the confocal images. All Lo tubes found

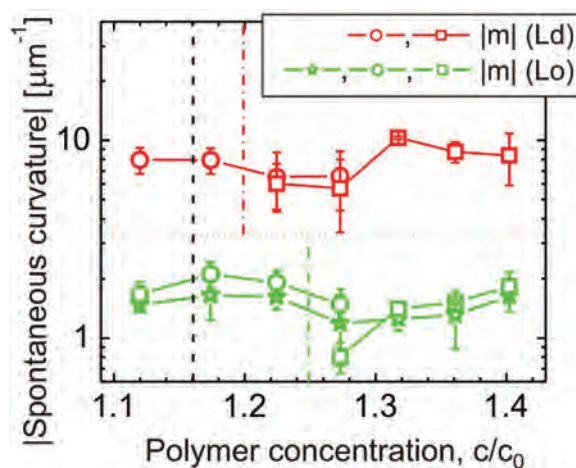


**Figure 7.** Absolute value of the spontaneous curvature as a function of the total polymer mass density  $c/c_0$  for Ld (red) and Lo (green) membranes with  $c_0 = 0.071 \text{ g cm}^{-3}$ . The vertical dashed line (black) indicates the critical concentration  $c_{cr} = 1.16 c_0$  which separates the aqueous one-phase from the two-phase region. The two vertical dashed-dotted lines (red at  $c/c_0 \approx 1.199$  and green at  $c/c_0 \approx 1.249$ ) separate the complete wetting from the partial wetting regimes for the Ld and Lo membranes. The data were obtained by direct shape analysis of the nanotubes (green stars), area partitioning analysis as given by Equation (1) (red and green open circles), and force balance analysis described by Equation (2) (red and green open squares). The horizontal dotted line corresponds to the optical resolution limit of  $1/(300 \text{ nm})$ . Adapted with permission.<sup>[7c]</sup> Copyright 2016, American Chemical Society.

for the VM-A and VM-B morphologies were relatively short and necklace-like, which implies that the spontaneous curvature  $m$  can be estimated via  $m = -1/\langle R_{ss} \rangle$  with the average radius  $\langle R_{ss} \rangle$  of the small, quasi-spherical beads. All  $m$ -values obtained by this direct shape analysis are displayed in Figure 7 as green stars. These values have an accuracy of about 20%, reflecting the relative standard deviation of the measured bead radius  $\langle R_{ss} \rangle$ .

The direct shape analysis was also applied to the cylindrical and necklace-like tubes coexisting on the Lo vesicle displayed in Figure 6. The average diameter  $\langle 2R_{cy} \rangle$  of the cylindrical tubes as obtained from the confocal scans implies the spontaneous curvature  $m = -1/\langle 2R_{cy} \rangle$ , which leads to  $m = -1.82 \text{ } \mu\text{m}^{-1}$ , with an accuracy of about  $\pm 13\%$  corresponding to the relative standard deviation of the measured diameter of the cylinder segments. The average bead diameter of the necklace-like tubes, on the other hand, leads to  $m = -1.56 \text{ } \mu\text{m}^{-1}$  with an accuracy of about  $\pm 19\%$ . The good agreement between the  $m$ -values obtained from the cylindrical and necklace-like tubes protruding from the same vesicle provided strong evidence that the spontaneous curvature was uniform along the whole membrane of the vesicle.

#### 5.2. Area Partitioning between Tubes and Mother Vesicle

For the Ld membranes, we could not resolve the shapes of the nanotubes because they had a diameter below optical resolution. However, we could still deduce the spontaneous curvature from two geometric quantities that can be directly determined from the confocal scans: the total tube area  $A = A_0 - A_{app}$  and the

total tube length  $L$ . The latter length can be estimated from the 3D confocal scans with an uncertainty of about  $\pm 15\%$ . All tubes with constant mean curvature are then characterized by spontaneous curvatures within the interval  $-2\pi L/A \leq m \leq -\pi L/A$ . Furthermore, if a fraction  $\Lambda$  of the total tube length is cylindrical and the remaining fraction  $1-\Lambda$  is necklace-like, we obtain the estimate

$$m = -(2-\Lambda) \frac{\pi L}{A} = -(2-\Lambda) \frac{\pi L}{A_0 - A_{\text{app}}} \quad (1)$$

For the VM-A and VM-B morphologies of the Lo membranes, all tubes had a necklace-like shape which implies  $\Lambda = 0$ . For the VM-C morphologies, on the other hand, tube adhesion can lead to some cylindrical tubes and nonzero  $\Lambda$ -values. The  $m$ -values obtained via Equation (1) are displayed in Figure 7 as green open circles and have an accuracy of  $\pm 15\%$ , the main uncertainty arising from the measurement of the tube length  $L$ .

For the Ld tubes, we could not estimate the fraction  $\Lambda$  from the confocal scans. However, the high flexibility of these tubes as observed for the VM-A and VM-B morphologies implied that these tubes were necklace-like as well. The same conclusion is obtained from the observed tube lengths, which are shorter than the critical tube lengths for the necklace-cylinder transformation. Therefore, we estimated the spontaneous curvatures for the VM-A and VM-B morphologies of the Ld membranes using Equation (1) with  $\Lambda = 0$ . For the VM-C morphologies of the Ld membranes, we deduced the total tube length  $L$  from the density of the tubes at the pd interface and estimated the spontaneous curvature via Equation (1) using both  $\Lambda = 0$  and  $\Lambda = 1$ , thereby taking the whole range  $0 \leq \Lambda \leq 1$  of possible  $\Lambda$ -values into account. The  $m$ -values obtained by this procedure are displayed in Figure 7 as red open circles.

### 5.3. Force Balance along the Contact Line for Partial Membrane Wetting

For the VM-C morphologies, the values of the spontaneous curvature as deduced from the direct shape and the area partitioning analysis could be validated via a third, completely different analysis method. The latter method is based on the interfacial tension  $\Sigma_{\text{pd}}$  of the pd interface as well as on the effective contact angles between the membranes, denoted by  $\theta_p$ ,  $\theta_d$ , and  $\theta_e$ , see Figure 2f, with  $\theta_p + \theta_d + \theta_e = \pi$ .<sup>[5b,7a]</sup> Using these quantities and the force balance along the contact line, one obtains the relation<sup>[7b]</sup>

$$m = - \left( \frac{\Sigma_{\text{pd}} \sin \theta_d}{2\kappa \sin \theta_e} \right)^{1/2} \quad (2)$$

for the spontaneous curvature where  $\kappa$  is the membrane's bending rigidity. Using the measured values for the bending rigidities,  $\kappa_{\text{Lo}}$  and  $\kappa_{\text{Ld}}$ , of the Ld and Lo membranes, the expression given by Equation (2) leads to  $m$ -values that are in good agreement with those obtained via the two other modes of analysis, see red and green open squares in Figure 7.

### 5.4. Deduced Values of the Spontaneous Curvature

Inspection of Figure 7 shows that the spontaneous curvatures of the Ld and Lo membranes were fairly constant over the range of polymer concentrations studied here, with  $m_{\text{Ld}} \cong -8 \mu\text{m}^{-1}$  and  $m_{\text{Lo}} \cong -1.7 \mu\text{m}^{-1}$ . As a consequence, the spontaneous curvature ratio  $m_{\text{Ld}}/m_{\text{Lo}}$  of the two types of membranes was found to be  $m_{\text{Ld}}/m_{\text{Lo}} \cong 4.7$ , which is approximately equal to the ratio  $\kappa_{\text{Lo}}/\kappa_{\text{Ld}} \cong 4.5$  of the corresponding bending rigidities. As we will see in the following section, the latter result agrees with theoretical predictions for the local curvature generation by polymer adsorption.

For both Ld and Lo membranes, the spontaneous curvature generates a spontaneous tension  $\sigma = 2\kappa m^2$ .<sup>[7b]</sup> Using the fluid-elastic parameters for the Ld and Lo membranes, we obtain the spontaneous tension  $\sigma = 1.28 \times 10^{-2}$  and  $0.261 \times 10^{-2} \text{ mN m}^{-1}$ , respectively. The latter tension contributes to the total membrane tension which is equal to the sum of the mechanical and the spontaneous tension. For the systems described here, the total tension is, in fact, dominated by the spontaneous tension reflecting the large magnitude of the spontaneous curvatures. More precisely, for the Ld and Lo membranes studied in ref. [7c] the theory in ref. [7b] implies that the mechanical tension is smaller than the spontaneous tension by a factor of  $3 \times 10^{-3}$  and  $1.5 \times 10^{-2}$ , respectively. Therefore, the mechanical tension is of the order of  $10^{-5}$  or  $10^{-4} \text{ mN m}^{-1}$ , several orders of magnitudes smaller than the tension of rupture which is of the order of a few  $\text{mN m}^{-1}$ .

## 6. Molecular Mechanism for Curvature Generation

Because vesicle tubulation was only observed in the presence of the polymers, the spontaneous curvature of the vesicle membranes must arise from the polymer-membrane interactions. If these interactions are effectively attractive or repulsive, the polymers form adsorption or depletion layers adjacent to the two bilayer leaflets. The membrane then prefers to bulge toward the solutions with the higher and lower concentrations for polymer adsorption and depletion, respectively.<sup>[21]</sup>

### 6.1. Negative Spontaneous Curvature for All Polymer Compositions

After the first deflation step, both the PEG and the dextran concentrations in the interior aqueous solution are larger than in the exterior solution. After the second and all subsequent deflation steps, the PEG concentration in the interior PEG-rich phase is again larger than in the exterior solution but the dextran concentration in the PEG-rich phase is now smaller than in this exterior solution. Furthermore, all deflation steps led to a negative spontaneous curvature of the membranes because all nanotubes were observed to protrude into the interior compartment of the vesicles. These observations are only consistent with the theoretical results in ref. [21a] if the spontaneous curvature is induced by PEG adsorption. The latter conclusion has been confirmed by additional experiments in which vesicles with the same lipid composition, were exposed to aqueous

solutions that contained only PEG and no dextran. For the latter systems, osmotic deflation of the vesicles by the addition of sucrose again generated membrane nanotubes that protruded into the interior solution with the higher PEG concentration.

### 6.2. PEG Adsorption Studied by Molecular Dynamics Simulations

To corroborate these conclusions about PEG adsorption and to obtain direct insight into the conformations of the adsorbed PEG molecules, atomistic molecular dynamics simulations of the polymer–lipid systems have been performed in ref. [7c] for the experimentally used lipid compositions and chain length of PEG. Typical conformations of adsorbed chains are displayed in Figure 8a,b for the Ld and Lo membranes, respectively. These conformations indicate that the PEG molecules are only weakly bound, with relatively short contact segments and relatively long loops in between. The two terminal OH groups of the PEG molecule were frequently bound to the membrane via hydrogen bonds. In addition, a small number of contacts was formed between the polymer backbones and the membranes. A more quantitative measure for the affinity of the polymers to the membranes is provided by the potentials of mean force as displayed in Figure 8c,d. These potentials indicate that the PEG molecules have essentially the same affinity for both types of membranes, with a binding free energy of about  $4 \text{ kJ mol}^{-1}$  or  $1.6 k_B T$  per polymer chain. This similarity is plausible because both phospholipid components of Ld and Lo membranes had the same PC head group.

It will be interesting to explore lipid mixtures with different head groups. For example, using sugar lipids such as gangliosides or PEGylated lipids, we may obtain enhanced membrane interactions with the dextran-rich or the PEG-rich phase, respectively. When exposed to the same PEG–dextran solutions, we expect to see both different bilayer affinities to the PEG molecules and different values for the intrinsic contact angle.

### 6.3. Ratio of Spontaneous Curvatures for Ld and Lo Membranes

The spontaneous curvature generated by adsorption of small and large molecules is theoretically predicted to be inversely proportional to the bending rigidity of the membrane<sup>[21]</sup> as recently confirmed for the adsorption of small molecules by molecular dynamics simulations.<sup>[22]</sup> If the PEG chains have similar affinities to the Ld and Lo membranes as observed in

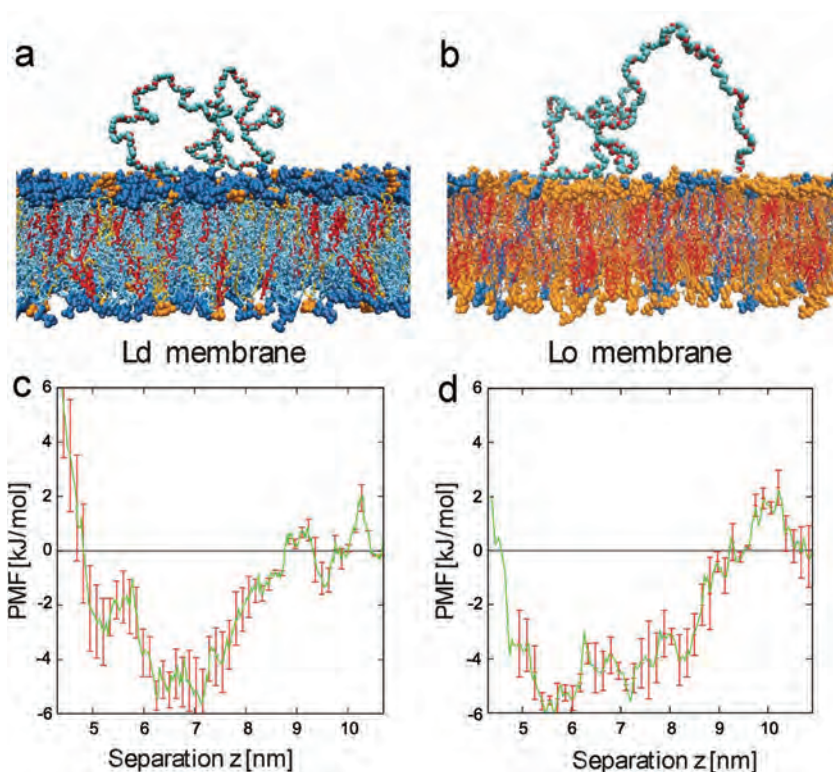


**Figure 8.** Typical conformation and potential of mean force for adsorbed PEG molecules: a,b) Simulation snapshots of PEG molecule adsorbed onto Ld and Lo bilayers. The lipid composition of the two types of membranes was the same as in the experiments. The color code for the lipids is blue for DOPC, orange for DPPC, and red for cholesterol. The PEG molecules consisted of 180 monomers corresponding to the average molecular weight used in the experiments. Each lipid membrane was immersed in about 27 000 water molecules (not shown) and c,d) potential of mean force (PMF) for Ld and Lo membranes as a function of the separation  $z$  between the polymer's center-of-mass and the bilayer midplane. The potential wells are relatively broad, with a width of about 4 nm, because the polymer end groups can adsorb even for relatively large  $z$ -values. The binding free energy of a single PEG chain is about  $4 \text{ kJ mol}^{-1}$  or  $1.6 k_B T$  for both types of membranes. Adapted with permission.<sup>[7c]</sup> Copyright 2016, American Chemical Society.

the molecular dynamics simulations, see Figure 8, the ratio  $m_{Ld}/m_{Lo}$  of the spontaneous curvatures should be equal to the ratio  $\kappa_{Lo}/\kappa_{Ld}$  of the bending rigidities. The latter rigidity ratio is estimated to be  $\kappa_{Lo}/\kappa_{Ld} \cong 4.5$ , based on the experimental results in ref. [18], which should be compared with the curvature ratio  $m_{Ld}/m_{Lo} \cong 4.7$  as obtained from the deflation experiments described in ref. [7c], see Figure 7. Because the experimental uncertainty is of the order of 10%–20% for both ratios, the data are consistent with  $m_{Ld}/m_{Lo} \cong \kappa_{Lo}/\kappa_{Ld}$  and, thus, with a comparable amount of adsorbed polymers on both types of membranes, in agreement with the simulation results.

From an intuitive point of view, the inverse proportionality between spontaneous curvature and bending rigidity can be understood as follows.<sup>[23]</sup> Consider a certain molecular mechanism acting on a small membrane segment that leads to a free energy gain proportional to the mean curvature  $M$  of this segment. When we balance this free energy gain  $\sim M$  with the bending energy  $\sim \kappa M^2$ , we obtain a preferred curvature  $M^* \sim 1/\kappa$  that can be identified with the spontaneous curvature.

## 7. Summary and Outlook on Related Processes

In summary, our studies of ATPS-loaded vesicles have shown that these systems exhibit interesting and unexpected behavior related to membrane wetting, droplet-induced (or wetting-induced) budding, and spontaneous tubulation. All of these phenomena are universal and can be present in any other system consisting of bilayer membranes and phase-separating aqueous solutions.

Wetting phenomena occur for any membrane that is exposed to two aqueous phases, irrespective of the molecular composition of the membranes and the aqueous solution. However, the molecular composition and the molecular interactions determine whether the membranes are wetted completely by one of the aqueous phases or wetted partially by both of them. For the PEG–dextran solutions studied here, both complete and partial wetting as well as complete-to-partial wetting transitions were observed, for several distinct lipid compositions of the membranes (Figures 2, 4, and 5). Furthermore, we also identified a hidden material parameter, the intrinsic contact angle that can be calculated from the effective contact angles as measured by optical microscopy.

As demonstrated in our studies, aqueous phase separation within a vesicle can be conveniently controlled by osmotic deflation of this vesicle. In addition to creating coexisting liquid droplets within the vesicle, the deflation process also reduces the overall volume of the vesicle. In general, the vesicle will then change its shape in order to minimize its bending energy under the constraint that it encloses (at least) two coexisting liquid droplets. One such shape transformation is provided by the droplet-induced (or wetting-induced) budding of the vesicle. However, after the interior phase separation process, the two leaflets of the vesicle membrane are typically exposed to an asymmetric environment, i.e., to two aqueous solutions that differ in their composition. As a consequence, the bilayer membrane acquires a certain asymmetry as quantitatively described by its spontaneous curvature. If this curvature is large compared to the inverse vesicle size, it leads to the formation of membrane nanotubes as observed for the PEG–dextran solutions and several lipid compositions. Because the formation of nanotubes arises from the spontaneous curvature, the tubulation process does not require aqueous phase separation and occurs already after the first deflation step for which the vesicle is still filled with a uniform aqueous solution.

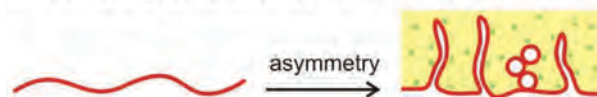
The formation of a membrane tube starts with the nucleation of a small membrane bud which then grows into a necklace-like tube. Because this nucleation and growth process typically starts from several nucleation sites on the vesicle membrane, the vesicle forms intricate patterns of nanotubes (Figure 5). When the length of a single tube reaches a certain critical value, the necklace-like tube transforms into a cylindrical one. As a consequence, short necklace-like and long cylindrical tubes can coexist on the same vesicle (Figure 6).

The theoretical analysis of the observed tube patterns leads to reliable estimates of the spontaneous curvature, both for Ld and Lo membranes. Our analysis is based on three different methods that examine three different aspects of the observed morphologies. All three methods give rather consistent results

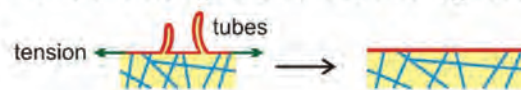
(Figure 7). The methods are rather general and can be applied to any system that exhibits spontaneous tubulation. Finally, a combination of (i) general theoretical considerations based on the polymer composition of the coexisting aqueous phases, (ii) detailed molecular dynamics simulations of the experimentally studied lipid composition and PEG molecules, and (iii) preliminary tubulation experiments with PEG alone leads to the conclusion that the spontaneous curvature is generated locally by weak PEG adsorption. Based on the molecular dynamics simulations, the binding affinity of the PEG molecules is found to be about  $4 \text{ kJ mol}^{-1}$  or  $1.6 k_B T$  per PEG chain, both for the Ld and Lo membranes (Figure 8). As a consequence, the ratio  $m_{Ld}/m_{Lo}$  of the two spontaneous curvatures is roughly equal to the inverse ratio  $\kappa_{Lo}/\kappa_{Ld}$  of the two bending rigidities. In this way, we were able to directly relate the membrane morphology as observed on the micrometer scale to the molecular interactions on the molecular scale. In particular, we could demonstrate that the weak adsorption of macromolecules can generate a substantial membrane curvature.

The physico-chemical processes described here—membrane wetting, droplet-induced budding, and spontaneous tubulation—are generic and, thus, should also affect the behavior of biological membranes. Possible cellular processes that involve spontaneous tube formation or partial membrane wetting are displayed in Figure 9. The first two panels of this figure illustrate the generation of curvature by asymmetric aqueous environments, the resulting tube formation, and the storage of membrane area within these tubes. Tubes could be relevant for the regulation of surface area in cells. Many cells, including growing neurons and dividing cells, undergo rapid volume and

### a Curvature generation by trans-membrane asymmetry



### b Membrane storage and surface area regulation



### c Wetting-facilitated endo/exo-cytosis

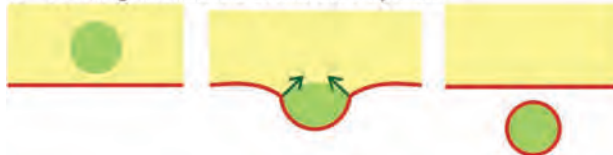


**Figure 9.** Possible cellular processes that involve membrane tubulation and/or aqueous phase separation: a) Tubulation of a biological membrane caused by an asymmetric aqueous environment (white and yellow); b) tubes represent an effective way of storing area, which can be retracted back via low (membrane or cortical) tensions. c) The spreading of a droplet (or membrane-less organelle) onto a biological membrane can initiate membrane budding during exo- or endocytosis. The budding process is facilitated by the tension of the interface between the two aqueous phases (yellow and green).

surface area change. These changes require a fast exchange of membrane between the surface and the internal membrane reservoirs. Tubes provide such reservoirs, from which the membranes can be easily recruited. The curvature generation leading to membrane shape modulation could arise from the asymmetric adsorption of proteins, see, for example, refs. [7b] and [24], in close analogy to the asymmetric adsorption of PEG molecules as described above. The example in Figure 9c displays membrane budding induced by a liquid-like droplet, a mechanism that could be used for the uptake of liquid-like droplets by membrane-bound organelles or during endo- and exocytosis of cell membranes. The droplets could represent membrane-less organelles, such as the nucleoli of *Xenopus laevis* oocytes and the cytoplasmic P granules of *Caenorhabditis elegans*, which have been recently observed to exhibit liquid-like properties: these organelles can attain spherical shapes and undergo droplet-like fusion.<sup>[25]</sup>

The structure and function of tubular membranous networks such as the trans-Golgi network and the smooth ER have been studied for a long time. However, the physical mechanism and driving forces involved in their formation and the remodeling of their membranes remain elusive. Tubular shapes in cells may be induced by actin polymerization<sup>[26]</sup> and molecular motors.<sup>[27]</sup> However, cytoskeletal filaments are not in abundance in the smooth ER. The phenomena observed in the model system of ATPS and GUVs reviewed here suggest that membrane restructuring in some cellular organelles can be governed by other mechanisms, namely, by the local generation of membrane curvature or by local phase separation in the crowded environment in the cell interior. Local concentration changes of macromolecules and/or phase separation could induce microcompartmentation by means of tube formation, whereby the spontaneous curvature stabilization may be assisted by proteins with banana-shaped domains or by lipids such as PI(3)P.

## Acknowledgements

This work is part of the MaxSynBio consortium which was jointly funded by the Federal Ministry of Education and Research of Germany and the Max Planck Society. The authors also acknowledge the collaboration with Y. Liu within the framework of the Partner Group Program of the Max Planck Society and the Chinese Academy of Sciences.

Received: May 17, 2016

Revised: July 22, 2016

Published online:

- [1] a) R. Dimova, in *Advances in Planar Lipid Bilayers and Liposomes* Vol. 16 (Ed: A. Iglič), Academic Press, Burlington, **2012**, pp. 1–50; b) R. Dimova, S. Aranda, N. Bezlyepkina, V. Nikolov, K. A. Riske, R. Lipowsky, *J. Phys. Condens. Matter* **2006**, *18*, S1151.
- [2] P. Å. Albertsson, *Partition of Cell Particles and Macromolecules: Separation and Purification of Biomolecules, Cell Organelles, Membranes, and Cells in Aqueous Polymer Two-Phase Systems and Their Use in Biochemical Analysis and Biotechnology*, 3rd ed., Wiley, New York **1986**.
- [3] M. R. Helfrich, L. K. Mangeney-Slavin, M. S. Long, Y. Djoko, C. D. Keating, *J. Am. Chem. Soc.* **2002**, *124*, 13374.
- [4] a) M. S. Long, C. D. Jones, M. R. Helfrich, L. K. Mangeney-Slavin, C. D. Keating, *Proc. Natl. Acad. Sci. USA* **2005**, *102*, 5920; b) L. M. Dominak, E. L. Gundermann, C. D. Keating, *Langmuir* **2010**, *26*, 5697; c) M. S. Long, A. S. Cans, C. D. Keating, *J. Am. Chem. Soc.* **2008**, *130*, 756.
- [5] a) Y. Li, R. Lipowsky, R. Dimova, *J. Am. Chem. Soc.* **2008**, *130*, 12252; b) H. Kusumaatmaja, Y. Li, R. Dimova, R. Lipowsky, *Phys. Rev. Lett.* **2009**, *103*, 238103; c) Y. Li, H. Kusumaatmaja, R. Lipowsky, R. Dimova, *J. Phys. Chem. B* **2012**, *116*, 1819.
- [6] M. Andes-Koback, C. D. Keating, *J. Am. Chem. Soc.* **2011**, *133*, 9545.
- [7] a) Y. Li, R. Lipowsky, R. Dimova, *Proc. Natl. Acad. Sci. USA* **2011**, *108*, 4731; b) R. Lipowsky, *Faraday Discuss.* **2013**, *161*, 305; c) Y. G. Liu, J. Agudo-Canalejo, A. Grafmuller, R. Dimova, R. Lipowsky, *ACS Nano* **2016**, *10*, 463.
- [8] H. Walter, D. E. Brooks, D. Fisher, *Partitioning in Aqueous Two-Phase Systems: Theory, Methods, Uses, and Application to Biotechnology*, Academic Press, Orlando, Florida, **1985**.
- [9] a) B. Y. Zaslavsky, *Aqueous Two-Phase Partitioning: Physical Chemistry and Bioanalytical Applications*, Marcel Dekker, New York, NY **1994**; b) R. Hatti-Kaul, *Aqueous Two-Phase Systems: Methods and Protocols*, Humana Press, Totowa, NJ, **2000**.
- [10] J. van der Gucht, E. Spruijt, M. Lemmers, M. A. C. Stuart, *J. Colloid Interface Sci.* **2011**, *361*, 407.
- [11] a) Y. Liu, R. Lipowsky, R. Dimova, *Langmuir* **2012**, *28*, 3831; b) J. Ryden, P. Å. Albertsson, *J. Colloid Interface Sci.* **1971**, *37*, 219; c) R. Dimova, R. Lipowsky, *Soft Matter* **2012**, *8*, 6409.
- [12] A. Kaul, *Aqueous Two-Phase Systems: Methods and Protocols*, Vol. 11, (Ed. R. Hatti-Kaul), Humana Press, Totowa, NJ, **2000**, pp. 11–21.
- [13] J. C. Merchuk, B. A. Andrews, J. A. Asenjo, *J. Chromatogr. B* **1998**, *711*, 285.
- [14] a) M. W. Edelman, R. H. Tromp, E. van der Linden, *Phys. Rev. E* **2003**, *67*; b) M. W. Edelman, E. van der Linden, R. H. Tromp, *Macromolecules* **2003**, *36*, 7783.
- [15] Z. L. Zhao, Q. Li, X. L. Ji, R. Dimova, R. Lipowsky, Y. G. Liu, *J. Chromatogr. A* **2016**, *1452*, 107.
- [16] a) A. S. Cans, M. Andes-Koback, C. D. Keating, *J. Am. Chem. Soc.* **2008**, *130*, 7400; b) C. D. Keating, *Acc. Chem. Res.* **2012**, *45*, 2114.
- [17] L. M. Dominak, C. D. Keating, *Langmuir* **2007**, *23*, 7148.
- [18] M. Heinrich, A. Tian, C. Esposito, T. Baumgart, *Proc. Natl. Acad. Sci. USA* **2010**, *107*, 7208.
- [19] U. Seifert, K. Berndl, R. Lipowsky, *Phys. Rev. A* **1991**, *44*, 1182.
- [20] R. Lipowsky, *Adv. Colloid Interface Sci.* **2014**, *208*, 14.
- [21] a) M. Breidenich, R. R. Netz, R. Lipowsky, *Mol. Phys.* **2005**, *103*, 3169; b) R. Lipowsky, H. G. Dobereiner, *Europhys. Lett.* **1998**, *43*, 219.
- [22] B. Rózycki, R. Lipowsky, *J. Chem. Phys.* **2015**, *142*, 054101.
- [23] R. Lipowsky, *Europhys. Lett.* **1995**, *30*, 197.
- [24] a) B. J. Peter, H. M. Kent, I. G. Mills, Y. Vallis, P. J. G. Butler, P. R. Evans, H. T. McMahon, *Science* **2004**, *303*, 495; b) S. Suetsugu, K. Murayama, A. Sakamoto, K. Hanawa-Suetsugu, A. Seto, T. Oikawa, C. Mishima, M. Shirouzu, T. Takenawa, S. Yokoyama, *J. Biol. Chem.* **2006**, *281*, 35347; c) A. Roux, G. Koster, M. Lenz, B. Sorre, J. B. Manneville, P. Nassoy, P. Bassereau, *Proc. Natl. Acad. Sci. USA* **2010**, *107*, 4141; d) B. R. Capraro, Y. Yoon, W. Cho, T. Baumgart, *J. Am. Chem. Soc.* **2010**, *132*, 1200; e) T. R. Graham, M. M. Kozlov, *Curr. Opin. Cell Biol.* **2010**, *22*, 430; f) T. Baumgart, B. R. Capraro, C. Zhu, S. L. Das, *Annu. Rev. Phys. Chem.* **2011**, *62*, 483; g) B. Sorre, A. Callan-Jones, J. Manzi, B. Goud, J. Prost, P. Bassereau, A. Roux, *Proc. Natl. Acad. Sci. USA* **2012**, *109*, 173; h) Z. Shi, T. Baumgart, *Nat. Commun.* **2015**, *6*, 5974.
- [25] a) C. P. Brangwynne, C. R. Eckmann, D. S. Courson, A. Rybarska, C. Hoegel, J. Gharakhani, F. Julicher, A. A. Hyman, *Science* **2009**,

- 324, 1729; b) C. P. Brangwynne, *Soft Matter* **2011**, *7*, 3052; c) C. P. Brangwynne, T. J. Mitchison, A. A. Hyman, *Proc. Natl. Acad. Sci. USA* **2011**, *108*, 4334; d) A. A. Hyman, K. Simons, *Science* **2012**, *337*, 1047.
- [26] a) D. Pantaloni, C. Le Clainche, M. F. Carlier, *Science* **2001**, *292*, 2012; b) A. Rustom, R. Saffrich, I. Markovic, P. Walther, H. H. Gerdes, *Science* **2004**, *303*, 1007.
- [27] a) A. Roux, G. Cappello, J. Cartaud, J. Prost, B. Goud, P. Bassereau, *Proc. Natl. Acad. Sci. USA* **2002**, *99*, 5394; b) G. Koster, M. VanDuijn, B. Hofs, M. Dogterom, *Proc. Natl. Acad. Sci. USA* **2003**, *100*, 15583; c) C. Leduc, O. Campas, K. B. Zeldovich, A. Roux, P. Jolimaître, L. Bourel-Bonnet, B. Goud, J. F. Joanny, P. Bassereau, J. Prost, *Proc. Natl. Acad. Sci. USA* **2004**, *101*, 17096.
-